DOI: 10.1007/s11661-007-9176-8

Crack-Tip Deformation Mechanisms in α-Fe and Binary Fe Alloys: An Atomistic Study on Single Crystals

PETER A. GORDON, T. NEERAJ, MICHAEL J. LUTON, and DIANA FARKAS

Molecular statics simulations are employed using semiempirical interatomic interaction potentials to examine the near crack-tip deformation mechanisms in iron and iron alloy single crystals under pure mode-I loading. The deformation mechanisms are found to be strong functions of the crack orientation. For pure Fe systems, the sensitivity of the overall response is explored by comparing the behavior of a number of recently developed potentials. The competition between ductile and brittle responses is interpreted between the well-known Griffith and Rice criteria, but is found to be lacking in predicting *a priori* the qualitative failure mechanism near the crack tip. The influence of Ni and Cr additions as ordered substitutional solutes is probed at concentrations up to 9.375 at. pct, and several qualitative differences in crack-tip behavior are observed.

I. INTRODUCTION

IT is a well-known experimental observation that the addition of solutes as dilute substitutional components in iron can impact important material properties such as flow stress, toughness, and the ductile-to-brittle transition temperature.[1,2,3] For these bcc metals, it is generally assumed that the yield stress of the material is controlled by the stress required to move screw dislocations, and the ductile-to-brittle transition temperature is sensitive to the strong temperature dependence of the screw dislocation motion. The precise mechanisms that explain this dependence are not well understood, although the presence of dissolved impurities is hypothesized to play a role.

In order to understand the influence of substitutional solutes in steels, molecular statics simulation was employed to examine the influence of Ni and Cr solutes on the failure mechanisms of atomically sharp microcracks in single crystals of ferrite. First, the effect of crack orientation on the response of cracks to mode-I loading in single crystals of pure iron was studied. This is in part motivated by a desire to examine in a single study a more comprehensive set of crack orientations than have been considered by previous authors.[4,5,6] The fracture behaviors of models based on a number of recently developed EAM potential models[7,8,9] were compared. This was carried out, in part, because previous studies appear to lead to differing conclusions about the intrinsic toughness of Fe depending on the potential employed. Finally, the influence of substitutional solutes on fracture behavior was studied using one of these model potentials. While it is not necessarily expected that these results can be directly applicable to explaining phenomena such as the ductile-to-brittle transition in alloys, they do provide insight into how solutes in ferrite can influence the competition at the crack tip between brittle cleavage and ductile emission in response to applied stress. The ultimate goal is to help aid in the understanding of the various ways that alloying additions can be used to improve the ductility of new steels.

PETER A. GORDON, Research Associate, T. NEERAJ, Senior Researcher, and MICHAEL J. LUTON, Senior Scientific Advisor, are with Corporate Strategic Research, ExxonMobil Research and Engineering, Annandale, NJ 08801. Contact e-mail: peter.a.gordon@exxonmobil.com DIANA FARKAS is with the Department of Materials Science and Engineering, Virginia Tech., Blacksburg, VA 24061.

This article is based on a presentation given in the symposium entitled "Deformation and Fracture from Nano to Macro: A Symposium Honoring W.W. Gerberich's 70th Birthday," which occurred during the TMS Annual Meeting, March 12–16, 2006, in San Antonio, Texas, and was sponsored by the Mechanical Behavior of Materials and Nanomechanical Behavior Committees of TMS.

II. METHODS

A. *Simulation of Mode-I Failure in Atomic Crystals*

To probe the failure mechanisms in single crystals, molecular statics simulations of mode-I (tensile) loading were conducted. Initially, single crystals of iron are generated in a rectangular simulation cell in an orientation where specific crystallographic directions line up with the simulation block axes. An idealized atomically sharp crack was then inserted into the simulation cell by application of the anisotropic displacement field obtained from linear elastic fracture mechanics (LEFM) under conditions of plane strain.[10] The crack was oriented such that the crack direction, crack plane normal, and crack front lay in the x, y, and z directions, respectively. The crack front direction was periodic, and the thickness was chosen to be at least twice the cutoff distance of the interaction potential.

The atoms in the simulation cell were divided into an inner "free" region, where atoms have no externally applied constraints, surrounded by a thin outer layer of fixed atoms, whose positions are dictated by the strain field given from LEFM. The initial stress intensity of the input crack was chosen to make sure the crack tip did not recede from its initial position. As long as the crack stabilized at its intended origin, the simulation results were not influenced by the precise value of the initial stress intensity of the crack.

During a statics simulation, the atoms in the free region were allowed to relax to their minimum energy configuration; convergence was deemed sufficient when the maximum gradient on any atom was below 10^{-4} eV/Å. From the initial input stress intensity, K_I, the crack was loaded by applying an incremental displacement field ($\Delta K_I = 0.016\ MPa\sqrt{m}$) to the atomic configuration derived from the previous loading step. This should be valid as long as the crack-tip origin does not deviate from its initial position. It is worth noting, however, that driving the crack in a

manner consistent with plane strain conditions neither enforces nor guarantees a plane-strain response in the simulation.[11] A more rigorous approach could be adopted by dilating the cell dimensions in x and y to satisfy the plane strain stress condition.[12] We expect this correction to have only a minor effect on our overall results.

The crystal orientations are chosen to offer the crack-tip favorable slip systems for dislocation emission. Since Fe has a bcc structure at low temperature, orientations were chosen to allow for {110}, {112}, and {123} slip planes to be available. It is notable that while this setup provides no driving force for emission of screw dislocations, mixed dislocations can be emitted. However, the loading can only drive the edge component of the burgers vector for emission, which biases the emission process in favor of pure edge dislocations. Table I lists the crystal orientations considered in this work, along with the geometric characterization of the most likely slip systems available for dislocation emission (as subsequently discussed).

The majority of simulation results presented here were performed on crystal blocks of approximately 130,000 atoms, with total block dimensions of 250 × 250 × 24Å, with the thin direction aligned with the crack front. Larger system sizes (up to 500,000 atoms) were also explored in selected cases to ensure that the overall crack-tip response was dictated by the system size. In all cases, the simulation results were identical.

For Fe-solute systems, it was found that random substitutions of solute in the lattice usually led to unstable configurations in terms of their elastic behavior. This is probably due to inadequacies in the Fe-solute potential function, whose development can only be viewed as approximate when applied in this context (as described in Section B). This leads to ambiguity in the choice of elastic constants with which to compute the displacement boundary conditions required to introduce the initial crack. To avoid this uncertainty, lattices with regular distributions of solute were employed. These systems were found to have well-defined behavior in the elastic (low strain) limit. To construct these arrays, a 4 × 4 × 4 bcc lattice with regular substitutions was employed. Labeling the coordinates of the atoms in the array (0, 0, 0), (a/2, a/2, a/2), (a, 0, 0), . . ., (7a/2, 7a/2, 7a/2), systems were constructed with solute content of 3.125 pct by substituting solutes at positions (2a, 2a, 2a) and permutations of (0, 2a, 0). Substitution at positions (a, a, a) and (3a, 3a, 3a) and permutations of (a, a, 3a) and (a, 3a, 3a) yielded an alloy composition of 6.25 pct. An alloy of 9.375 pct solute, then, can be generated as the sum of the previous two cases. Crack simulations at each of these compositions were performed for the orientations listed in Table I for both Cr and Ni.

Table I. Summary of Orientations Considered for Mode I Crack Propagation Simulations

System	Block Orientation (Crack Plane) [Crack Direction]	Slip Systems	θ (deg)	ϕ
1	(001)[110]	{112}⟨111⟩	±35.3	0
		{110}⟨111⟩	±90	±54.7
2	(110)[001]	{112}⟨111⟩	±54.7	0
		{112}⟨111⟩	±125.3	0
3	(111)[11$\bar{2}$]	{112}⟨111⟩	±90	0
		{112}⟨111⟩	−19.5	0
		{110}⟨111⟩	35.3	±54.7
4	(111)[$\bar{1}$10]	{110}⟨111⟩	±90	0
		{132}⟨111⟩	±22.2	±28.1
5	(0$\bar{1}$1)[011]	{110}⟨111⟩	±90	±35.3

B. *Potentials*

The simulations in this study employed the embedded-atom model (EAM) potential to describe the interactions of Fe and the Ni and Cr solutes. The general form of this function for single component systems is

$$E_{\text{tot}} = \sum_i \sum_{j>i} V_{\text{pair}}(r_{ij}) + \sum_i F(\rho_i)\rho_i = \sum_{j\neq i} \phi(r_{ij}) \qquad [1]$$

where the total energy is divided into a radially symmetric pair energy term V_{pair}, and $F(\rho_i)$, a volume-dependent embedding energy term. The latter is a function of ρ_i, the total electron density centered at atom i due to the surrounding atoms. The electron density, ρ_i, is computed as a pairwise summation of the local electron density contribution $\phi(r_{ij})$, summed over neighbors. For multicomponent systems, additional functions describing pair interactions between unlike species are required, as well as species-specific embedding and electron density functions.

A number of different workers have developed potentials of this type to describe iron. The potential of Simonelli and co-workers[13] was fitted to reproduce basic crystal properties including the elastic constants, perfect crystal cohesive energy, and vacancy formation energy of the bcc phase. The potential of Ackland *et al.*[7] was fitted to similar properties, but employs a Finnis–Sinclair embedding energy function, $F(\rho_i)=\sqrt{\rho_i}$. Mendelev *et al.*[9] employed a broader range of properties with which to fit their potential, including self-interstitial energies and *ab initio* forces computed on approximate liquid state configurations. This strategy was used based on the assumption that probing a wider range of the interatomic distances would lead to a more robust potential description. Using a variety of different self-consistent fitting strategies, Mendelev *et al.*[9] derived a number of potentials. Two of these are judged to be better able to reproduce a wide range of material properties and are tested in this work. These potentials are denoted herein as Mendelev-II[9] and Mendelev-IIext.[8]

The EAM potential is invariant to the following transformations:[14,15]

$$\phi_i(r_{ij}) \Rightarrow s\phi_i(r_{ij})\ F(\rho_i) \Rightarrow F(\rho_i/s) \qquad [2]$$

$$F(\rho_i) \Rightarrow F(\rho_i) + q\rho_i\ V_{\text{pair}}(r_{ij}) \Rightarrow V_{\text{pair}}(r_{ij}) - 2q\phi(r_{ij}) \qquad [3]$$

where s and q are arbitrary constants. When q is chosen to be the derivative of the embedding energy evaluated at the perfect lattice electron density, $q = -F'(\rho_0)$, the transformation of Eq. [3] is referred to as the effective pair scheme. Using these transformations, the four Fe potentials are plotted on a comparable basis in Figure 1. Several properties of Fe single crystals were computed with each of these potentials and are displayed in Table II. It is clear that

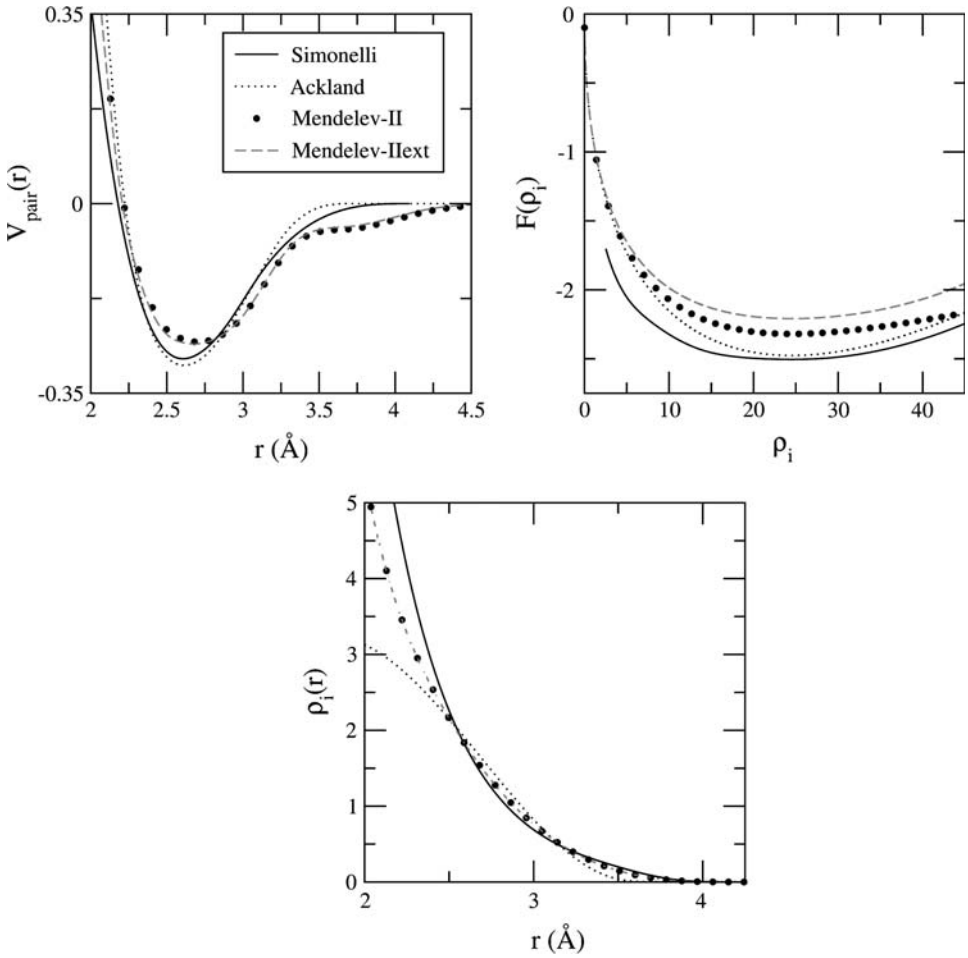

Fig. 1—Comparison of Fe-EAM potentials used in this work. For ease of comparison, the potentials are transformed to an effective pair format, and the embedding energy is scaled for all cases such that the minimum occurs at the same value, 24.5.

significant differences exist among the potential functions, even though they all reproduce the lattice constant and elastic constants of the perfect crystal with roughly equal accuracy.

To examine the influence of Ni and Cr solutes in binary mixtures with Fe, potentials built upon the potential of Simonelli[13] were employed. For Ni, the EAM description of Voter[14] was used. The additional Fe-Ni pair potential was obtained by an empirical fit to a simple interpolating function based on the pure species potential functions, with the requirement that the disordered 50/50 fcc phase is stable.[16] The EAM Cr potential used here is also due to Farkas *et al.*[15] The Fe-Cr pair function was determined by fitting to heats of mixing of Fe-Cr alloys and available data on the change of the lattice parameter of Fe due to Cr additions.

C. *Griffith Cleavage vs Rice Emission Criteria*

At the atomic level, a brittle or ductile response of an atomically sharp crack tip to externally applied stresses can be viewed as a competition between the cleavage of surfaces and the emission of dislocations through the shearing of adjacent atomic layers. Rice[17] proposed a dislocation nucleation criterion based on the Peierls concept; for two planes shearing past each other; the energy of the system is assumed to be a periodic function of the sliding distance. The applied stresses necessary to nucleate a dislocation can then be related to an energy barrier that must be overcome during the sliding process. Rice defined a quantity called the unstable stacking fault energy, γ_{us}, as an approximate measure of a material's intrinsic resistance to dislocation emission. This quantity is clearly a function of the particular slip plane and direction of sliding.

The Rice analysis considered externally applied stress in modes I, II (in-plane shear), and III (out-of-plane shear) loading. Here, where only pure mode I loading is considered, the energy release rate is given as

$$G_{\text{emit}} = \gamma_{us} \frac{1 + (1 - \nu) \tan^2 \phi}{f_I^2(\theta)} \qquad [4]$$

where ν is the Poisson ratio, θ is the angle between the slip plane and the crack plane, and ϕ is the angle between the dislocation burgers vector in the slip plane under consideration and the vector perpendicular to the crack front in the slip plane. The dimensionless quantity $f_I(\theta)$ is the θ-dependent portion of the shear stress resolved on the slip plane:

$$f_I(\theta) = \sigma_{xy} \cos(2\theta) + \frac{\sigma_{yy} - \sigma_{xx}}{2} \sin(2\theta) \qquad [5]$$

which can be obtained from the continuum LEFM analysis of the stress fields around a mode-I crack. This quantity is then compared to the energy release rate at the critical Griffith stress for brittle cleavage, which is simply related to the surface energy, γ_s, of the crystal surface on which the crack will open:

$$G_{Gr} = 2\gamma_s. \quad [6]$$

Accordingly, the system would be expected to emit a dislocation, thereby blunting the crack tip, when $G_{\text{emit}} < G_{\text{Gr}}$.

An advantage of the Rice theory is the relative ease of its application; the fate of a crack should be predictable by knowledge of two material parameters, the surface energy of available cleavage planes and the unstable stacking fault energies for available slip systems. These quantities were computed for the EAM potentials used in this work and are shown in Table II. The unstable stacking fault energies are computed for the known slip systems in bcc crystals, following the methodology of Farkas *et al.*[18]

In addition, it is useful to be able to compare the stress intensities at which events occur (either brittle crack advance or dislocation emission) in the simulations to those predicted by the Griffith and Rice criteria; the latter are defined by the relationships

$$K_{\text{Gr}} = \sqrt{\frac{G_{\text{Gr}}}{A_1}}$$
$$K_{\text{emit}} = \sqrt{\frac{G_{\text{emit}}}{A_2}} \quad [7]$$

where A_1 and A_2 modes I and II moduli (in terms of the plane-strain moduli, a_{ij} for the orientation under consideration).[10]

$$A_1 = \left[\sqrt{\frac{a_{11}a_{22}}{2}}\sqrt{\frac{\sqrt{\frac{a_{22}}{a_{11}}} + 2a_{12} + a_{66}}{2a_{11}}}\right]^{-1}$$
$$A_2 = \left[\frac{a_{11}}{\sqrt{2}}\sqrt{\sqrt{\frac{a_{22}}{a_{11}}} + \frac{2a_{12} + a_{66}}{2a_{11}}}\right]^{-1} \quad [8]$$

III. RESULTS AND DISCUSSION

A. *Iron Single Crystals*

For each mode-I loading simulation conducted, the initial loading conditions, the stress intensity of critical events, and a description of the event type are summarized in Tables III through VII. Also listed are the predicted Griffith

Table II. Computed Properties of EAM Fe Potentials Employed in This Work.

Potential	a_0(Å)	E_{coh}(eV/Atom)	C_{11}	C_{12}(Gpa)	C_{44}	Plane	γ_s(J/m^2)	γ_{us}
Simonelli	2.8668	−4.28	242.5	145.7	112.4	{112}	1.70	0.865
						{110}	1.44	0.741
						{123}	1.65	0.850
						{100}	1.63	
						{111}	1.80	
Ackland	2.8665	−4.316	242.8	145.0	116.0	{112}	1.89	1.044
						{110}	1.58	0.895
						{123}	1.84	1.025
						{100}	1.81	
						{111}	2.00	
Mendelev-II	2.8553	−4.122	244.2	144.4	116.2	{112}	1.91	0.770
						{110}	1.65	0.663
						{123}	1.87	0.755
						{100}	1.79	
						{111}	2.00	
Mendelev-IIext	2.8553	−4.013	243.1	144.6	116.2	{112}	1.87	0.775
						{110}	1.62	0.672
						{123}	1.83	0.765
						{100}	1.75	
						{111}	1.96	

Table III. Summary of Mode I Loading Simulations for Orientation 1: the {001}⟨110⟩ Crack

	$K_{I,\text{initial}}$	$K_{J,\text{event}}$		K_{Gr}	$K_{I,\text{emit}}$	
Potential	(MPa$\sqrt{m}$)		Event Type	(MPa$\sqrt{m}$)		Crack Plane/Slip System
Simonelli	0.87	0.93	brittle	0.85	1.70	{001}
Ackland	0.88	1.06	brittle	0.91	1.89	{001}
Mendelev-II	0.85	1.07	brittle	0.96	1.62	{001}
Mendelev-IIext	0.85	1.09	brittle	0.95	1.60	{001}

Table IV. Summary of Mode I Loading Simulations for Orientation 2: the {110}⟨001⟩ Crack

Potential	$K_{I,\text{initial}}$ (MPa$\sqrt{m}$)	$K_{I,\text{event}}$ (MPa$\sqrt{m}$)	Event Type	K_{Gr} (MPa$\sqrt{m}$)	$K_{I,\text{emit}}$ (MPa$\sqrt{m}$)	Crack Plane/Slip System
Simonelli	0.82	0.96	ductile	0.85	1.22	{112}⟨111⟩
Ackland	0.82	1.09	ductile	0.90	1.17	{112}⟨111⟩
Mendelev-II	0.82	1.33	ductile	0.93	1.15	{112}⟨111⟩
Mendelev-IIext	0.82	1.14	brittle	0.91	1.15	{110}

Table V. Summary of Mode I Loading Simulations for Orientation 3: the {111}⟨112⟩ Crack

Potential	$K_{I,\text{initial}}$ (MPa$\sqrt{m}$)	$K_{I,\text{event}}$ (MPa$\sqrt{m}$)	Event Type	K_{Gr} (MPa$\sqrt{m}$)	$K_{I,\text{emit}}$ (MPa$\sqrt{m}$)	Crack Plane/Slip System
Simonelli	0.87		twin	0.93	1.33	{112}⟨111⟩
Ackland	0.87		twin	0.98	1.44	{112}⟨111⟩
Mendelev-II	0.90		twin	0.99	1.27	{112}⟨111⟩
Mendelev-IIext	0.90		twin	0.99	1.27	{112}⟨111⟩

Table VI. Summary of Mode I Loading Simulations for Orientation 4: the {111}1⟨110⟩ Crack

Potential	$K_{I,\text{initial}}$ (MPa$\sqrt{m}$)	$K_{I,\text{event}}$ (MPa$\sqrt{m}$)	Event Type	K_{Gr} (MPa$\sqrt{m}$)	$K_{I,\text{emit}}$ (MPa$\sqrt{m}$)	Crack Plane/Slip System
Simonelli	0.87	1.06	ductile	0.91	1.22	{110}⟨111⟩ and {132}⟨111⟩
Ackland	0.90	1.25	ductile	0.96	1.35	{110}⟨111⟩
Mendelev-II	0.90	1.28	ductile	0.98	1.17	{110}⟨111⟩
Mendelev-IIext	0.90	1.15	ductile	0.96	1.17	{110}⟨111⟩

Table VII. Summary of Mode I Loading Simulations for Orientation 5: the {011}⟨011⟩ Crack

Potential	$K_{I,\text{initial}}$ (MPa$\sqrt{m}$)	$K_{I,\text{event}}$ (MPa$\sqrt{m}$)	Event Type	K_{Gr} (MPa$\sqrt{m}$)	$K_{I,\text{emit}}$ (MPa$\sqrt{m}$)	Crack Plane/Slip System
Simonelli	0.87	1.12	brittle	0.78	1.41	{110}
Ackland	0.85	1.39	brittle	0.82	1.55	{110}
Mendelev-II	0.85	1.15	brittle	0.83	1.35	{110}
Mendelev-IIext	0.85	1.19	brittle	0.83	1.36	{110}

stress intensity and the lowest stress intensity for ductile emission (corresponding to the slip system listed in bold in Table I) based on the Rice unstable stacking fault analysis. In addition, Figures 2 through 4 show several representative configurations visualized with AtomEye[19] after a ductile response.

For orientations 1 and 5, all four Fe potentials considered exhibited brittle cleavage. For orientation 1, the crack cleaves on the (100) plane. The stress intensities for cleavage observed are generally about 10 to 15 pct higher than that predicted by the Griffith criterion. However, the relative changes among the potentials appears to be consistent with the trends in {100} surface energies. For instance, the Simonelli potential has the lowest γ_s (1.63 J/m^2), while the remaining three potentials are notably higher. It might be expected that the ratio of cleavage stress intensities varies as $\sqrt{\gamma_{s,a}/\gamma_{s,b}}$. However, the stress intensity ratio between the Simonelli and Ackland potential is expected to be approximately 1.05, while it is observed to be 1.14.

Simulations for orientation 5 all cleaved along the {110} plane. The stress intensity required to trigger this event is much higher than that given by the Griffith cleavage criterion. The Ackland potential exhibited the largest overprediction, and was noticeably higher than the other three models. These trends did not mirror the trends in surface energy on the (110) plane, where γ_s is ranked as Simonelli $<$ Ackland $<$ Mendelev $\approx$ Mendelev-IIext. In both orientations 1 and 5, it is noted that compared to the most favorable slip system available, the predicted stress intensity for emission far exceeds the cleavage limit, which is consistent with the universally brittle response observed in these orientations.

In orientation 2, systems described by the Simonelli, Ackland, and Mendelev-II potentials all exhibit a ductile first event, emitting a perfect ⟨111⟩ edge on the {112} plane $\theta = 54.7$ deg from the crack plane (Figure 2). A comparison of the predicted K_{Gr} and K_{emit} stress intensities, shown in Table IV, does not anticipate a ductile response. In fact, K_{Gr} predicts cleavage along the {110} plane at values

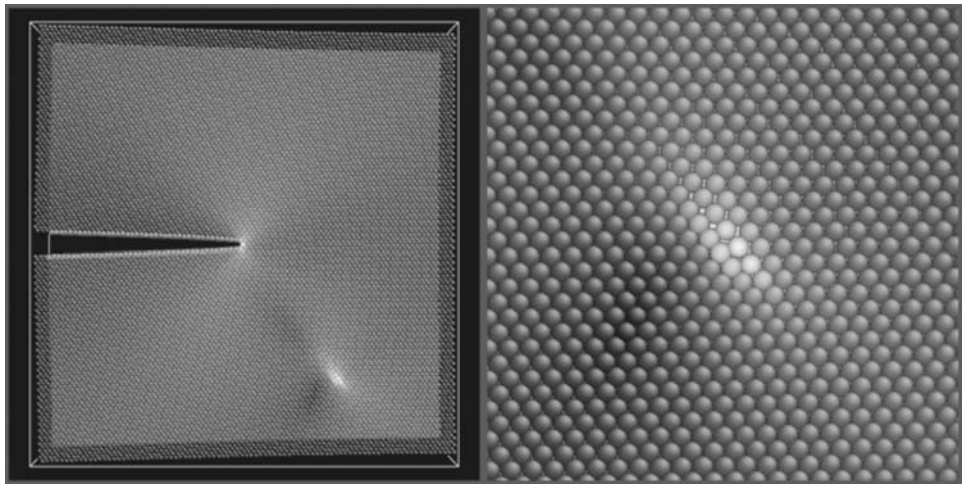

Fig. 2—Configuration of the ductile response of Simonelli potential in orientation 2 at $K_I = 0.96$ MPa$\sqrt{m}$. The figure at right zooms in to display the $\{112\}\langle 111\rangle$ dislocation emitted on the plane −54.7 deg from the crack plane. Atom colors are grayscaled according to the local Von-Mises stress, ranging from black (low) to white (high).

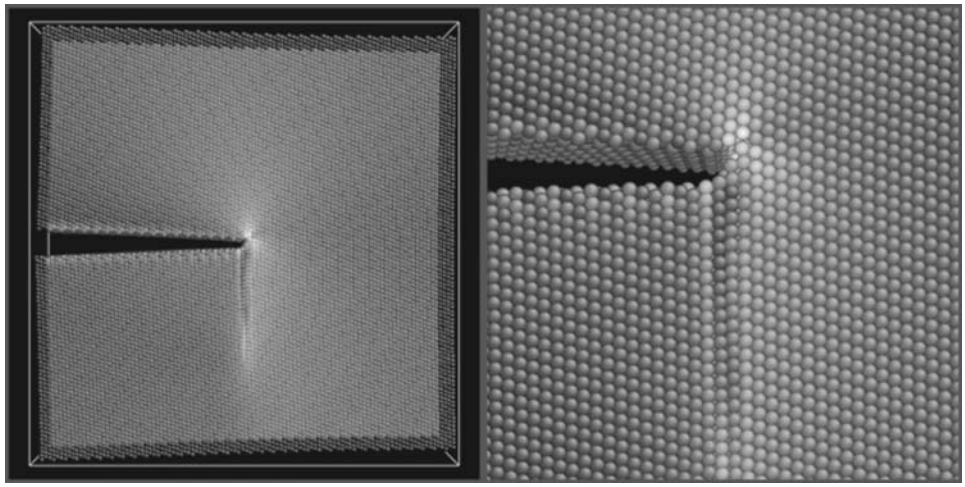

Fig. 3—Configuration of ductile response of Simonelli potential in orientation 3 at $K_I = 1.15$ MPa$\sqrt{m}$. The figure at right zooms in to display the $\{112\}\langle 111\rangle$ mechanical twin formed on the plane −90 deg from the crack plane, along with the brittle cleavage advance on the $\{110\}$ plane at 35.3. Atoms are colored as in Fig. 2.

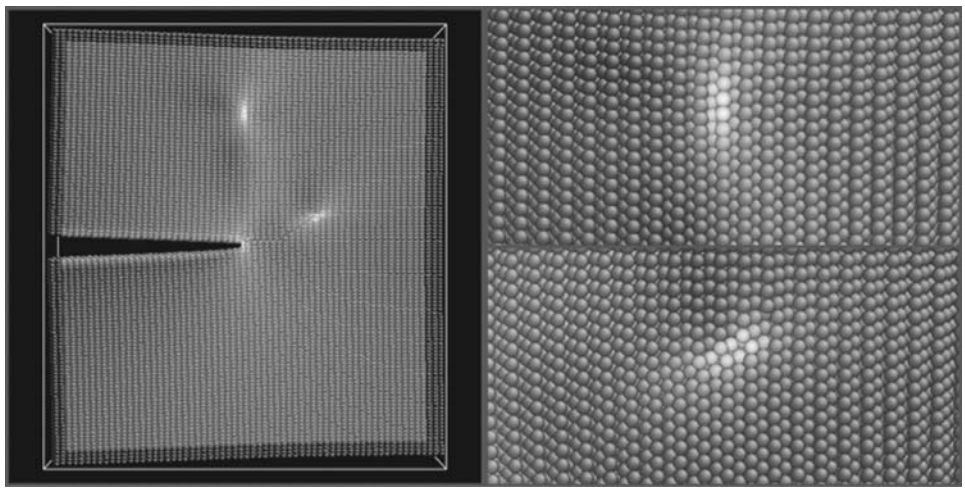

Fig. 4—Configuration of ductile response of Simonelli potential in orientation 4 at $K_I = 1.06$ MPa$\sqrt{m}$. The figures zoom in to display (upper) the $\{110\}\langle 111\rangle$ edge dislocation at 90 deg, and (lower) the mixed $\{132\}\langle 111\rangle$ dislocation at −28.1 deg from the crack plane. Atoms are colored as in Fig. 2.

below that required to trigger the observed ductile event. Somewhat surprisingly, the Mendelev-IIext potential produces a qualitatively different result, exhibiting brittle cleavage along the crack plane. In this case, however, the observed cleavage stress intensity is nearly 25 pct higher than the Griffith value. That the Mendelev-II and Mendelev-Ilext potentials, derived from nearly identical input data and nearly identical in predictions of many material properties, produce different qualitative results is evidence of the extreme sensitivity of the crack-tip response to the potential model description.

In orientation 3, all systems exhibited the growth of a mechanical twin on the {112} plane oriented at $\theta = -90$ deg from the crack plane, as shown in Figure 3. In all cases except the Ackland potential model, the twin was observed to grow until a critical stress intensity above which the crack advanced by cleavage on the {110} plane at $\theta = 35.3$ deg. The Griffith stress intensity for cleavage on this plane was estimated following Hoagland,[11] where it is assumed that, for low-angle departure from the crack plane,

$$K_{Gr}(\theta) = \frac{K_{Gr}}{\sqrt{cos\ \theta}} \qquad [9]$$

It is difficult to assign a unique value of the stress intensity at which the mechanical twin first emerges; however, it is clear by examination of Table V that the K_{Gr} and K_{emit} stress intensities would suggest a brittle response of the system.

All systems exhibit a ductile response in orientation 4, emitting an edge dislocation along the {110} plane. The Simonelli potential is the only model that produced the simultaneous emission of a mixed dislocation on the {132} plane at the first event, as shown in Figure 4. Again, the computed K_{Gr} stress intensity is somewhat lower than the K_{emit}.

The following observations can be made regarding the results of this simulation study. First, it is clear that a wide variety of different crack-tip responses occur for the range of crack orientations studied. In addition to brittle cleavage on the most favored {100} and {110} planes, pure edge and mixed dislocations can be activated on the {112}⟨111⟩, {110}⟨111⟩, and {132}⟨111⟩ slip systems, as well as the formation of a {112}⟨111⟩ mechanical twin. Furthermore, despite the differences in the parameterization procedures and development of the various potentials considered, the overall behavior is relatively uniform. There are some differences in terms of the stress intensities at which crack propagation or emission takes place, but the qualitative behavior in almost all cases is the same.

In terms of quantitative comparison, it is found that the continuum-based treatments that produce estimates for predicting the stress intensities for brittle or ductile crack response are only semiquantitative in nature. In orientations 1 and 5, all simulations produced brittle crack extension, but always at a stress intensity greater than K_{Gr}. This can be attributed to the phenomenon of lattice trapping,[20] where an activation energy barrier for crack advance still exists at a range of stress intensities above the Griffith value, thereby preventing brittle fracture at the anticipated thermodynamic limit. The degree of lattice trapping is often characterized by $R = K_{\mathrm{cleave}}/K_{\mathrm{Gr}}$, the ratio of stress intensity at which the crack advances to that of the Griffith value.[21] In orientation 1, R ranges from 1.09 to 1.16, while in orientation 5, it varies from 1.38 to 1.71. Where the degree of lattice trapping is small, as in orientation 1, the relative ratios in K_{cleave} follow the trends in the surface energy of the fracture surface. Where lattice trapping effects are large, as in orientation 5, this is no longer the case.

The large dependence of R on the crack plane is consistent with other work on Fe potentials, where both crack plane type and propagation direction were observed to influence the degree of lattice trapping.[22] The lattice trapping phenomenon has been shown to be related to the differing length scales involved in cutting the bonds at the crack tip and elastically relaxing the crack-tip region. Furthermore, the degree of lattice trapping can be quite sensitive to the details of the potential model employed.[23] In order to produce an improved cleavage threshold prediction, a more detailed analysis of the cleavage activation energy barriers needs to be conducted.

In most cases, the predicted stress intensity, K_{emit}, for ductile emission tends to be somewhat larger than is observed in the simulations. This has been noted in similar statics simulations on finite-sized cracks using the Simonelli potential.[6] One possible explanation is the influence of surface stresses near the crack tip; the elastic distortion of the surface near the crack-tip may dramatically influence the barriers for emission. A modified emission criterion that incorporates surface stress has been formulated,[24] although simulations on many fcc metals described with EAM models suggest this effect serves to *increase* the predicted emission stress. To our knowledge, no studies have been carried out on bcc materials that attempt to characterize this effect. It is also notable that this effect cannot be explained by the incorporation of an extra ledge creation energy penalty,[25] because that would only increase the discrepancy between the atomistic simulation and the continuum prediction.

Another plausible explanation for the overprediction of the Rice emission model is the omission of tension–shear stress coupling on slip planes present in mode-I loading. A strong tensile stress component across available slip planes could reduce the sliding resistance barriers for dislocation emission.[5] Sun and co-workers[26] formulated a model that relates shear and normal stresses along a potential slip plane as a function of displacements both parallel and perpendicular to the plane. In addition to the unstable stacking fault energy, this requires the characterization of an additional material parameter, namely, the magnitude of atomic displacement perpendicular to the slip plane to achieve zero tensile stress when the shear displacement is b/2, the point at which the unstable stacking fault energy is defined. For a different Fe potential, Sun *et al.*[26] demonstrated that for the {110}⟨111⟩ slip system at various combinations of $\{\theta, \phi\}$, the energy release rate decreased by approximately 30 pct over predictions without tensile stress coupling. This magnitude seems insufficient to reconcile the magnitude of over-prediction observed here, but it is noted that different potential models yield very different unstable stacking fault energies.

To assess this effect, unstable stacking fault energies on the {110}, {123}, and {112} planes were computed in the presence of a uniform applied normal strain field for each of the potentials considered here. At normal strains above

approximately 0.01, it was found that γ_{us} starts to decrease. An example of this for the $\{110\}\langle 111\rangle$ slip system is depicted in Figure 5, which plots the relative energy profiles against sliding distance for three different potentials. Note that the rate of decrease in γ_{us} with increasing applied strain is quite model dependent. The other slip systems show similar behavior. Although no attempt was made to directly compute the resolved stress on particular slip planes in our simulations, it is estimated that the near-crack-tip stresses are large enough to reduce the value of γ_{us} by 20 to 40 pct for the slip systems with a sizable normal stress component. Of course, this mechanism would not have any effect on slip systems at $\theta = \pm 90$ deg, where no stress normal to the potential slip plane should be present. For the Simonelli potential in orientations 2 through 4, a reduction in γ_{us} by a factor of roughly 2 would be required for the Rice criterion to predict a ductile response. Thus, tensile stress coupling effects alone seem insufficient to reconcile the degree of overprediction given by the Rice model for the systems studied.

B. *Effect of Solute Additions*

Although the combined Rice and Griffith criteria appear only to be capable of semiquantitative prediction of the competition between ductile and brittle failure, the analysis can still be of use in understanding relative changes from a given reference system.

The effects of Ni and Cr additions on basic material properties are shown in Table VIII for ordered structures up to 9.375 at. pct. The surface energies now depend on the precise plane that is cleaved, and, where possible, we have performed the calculations on the same atomic layers that form the crack plane in the mode I loading simulations. It is clear from the results, however, that the Ni additions have almost no effect on the surface energies, while Cr generally decreases γ_s on both the {110} and {100} planes. It was not convenient to compute the unstable stacking fault energies on the exact slip planes activated in the fracture simulations. Instead, we performed these calculations on systems with random solute substitutions up to 10 mol pct. For both Ni and Cr, the effect on γ_{us} was similar for the {112}, {110}, and {123} slip planes; at x_{solute}

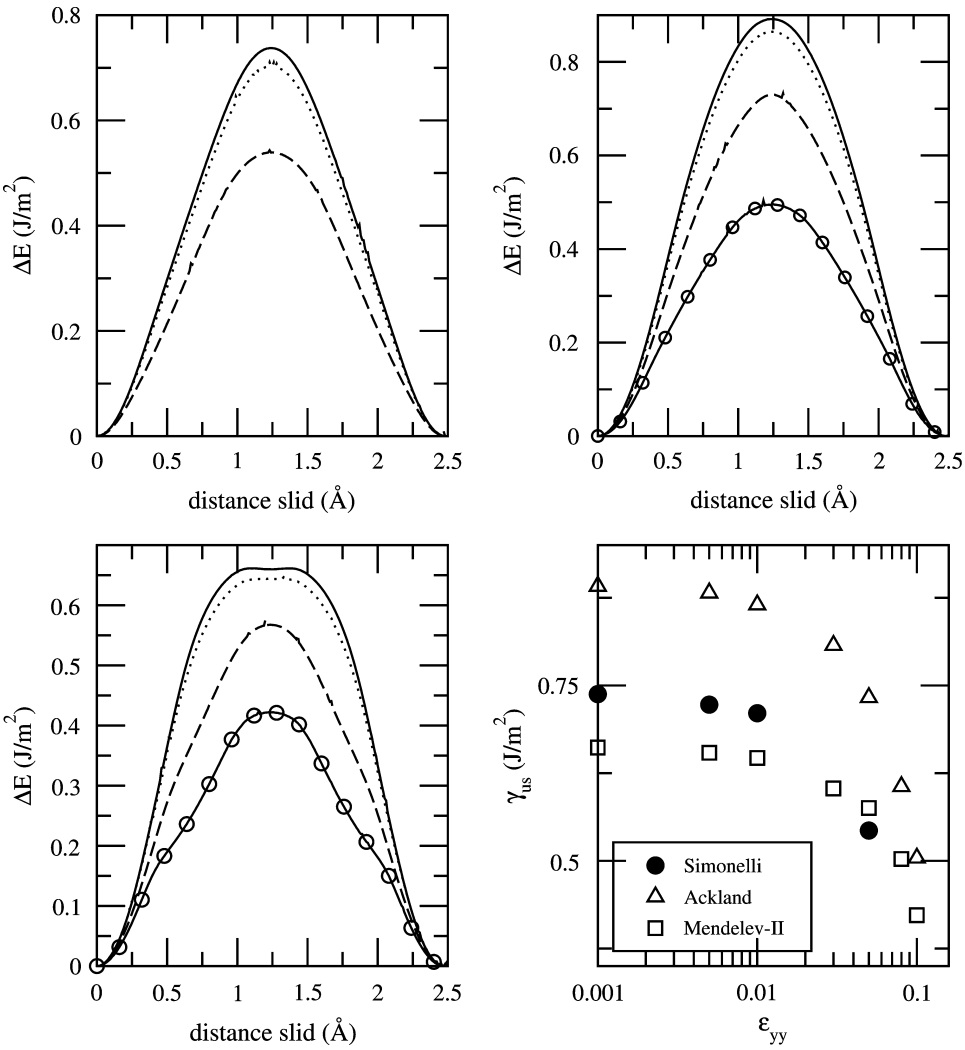

Fig. 5—Relative energy *vs* sliding profiles of the $\{110\}\langle 111\rangle$ slip system with varying amounts of homogeneous strain applied normal to the sliding surface. (—) $\varepsilon_{yy} = 0.001$, (. . .) $\varepsilon_{yy} = 0.01$, (- - -) $\varepsilon_{yy} = 0.05$, and (◆ ◆ ◆) $\varepsilon_{yy} = 0.1$. Upper left: Simonelli potential, upper right: Ackland potential, lower left: Mendelev-II potential, and lower right: summary of unstable stacking fault energies *vs* applied strain for each potential.

of 0.10, the unstable stacking fault energies decrease by approximately 5 to 6 pct. It is worth noting that the variation in γ_{us} with solute content was not very sensitive to repeated calculations with different random solute distributions.

In the first two orientations, little effect was noted with the addition of Cr or Ni. Orientation 1 remained brittle in all cases, with only a slight decrease (3 to 4 pct) in the stress intensity at cleavage. Similarly, ductile orientation 2 always emitted an edge dislocation on the {112} plane and increasing solute concentration resulted in a slight decrease (3 to 4 pct) in the stress intensity at emission.

In several other orientations, the presence of solutes gave rise to qualitative differences in the crack-tip response. In orientation 3, the pure Fe system displayed the growth of a mechanical twin followed by brittle cleavage along the {110} plane, as depicted in Figure 3. Figure 6 shows a

Table VIII. Effect of Cr and Ni Addition on Material Properties in Simonelli Fe

x_{Ni}	a_0 (Å)	C_{11}	C_{12} (GPa)	C_{44}	γ_s,100	γ_s,100 (J/m^2)	γ_s,123
0.0	2.8668	242.5	145.7	112.4	1.44	1.63	1.65
0.03125	2.8663	239.8	146.5	110.6	1.42	1.62	1.61
0.06250	2.8658	234.6	145.0	107.9	1.45	1.63	1.63
0.09375	2.8653	239.2	144.3	105.9	1.43	1.62	1.64
x_{cr}	a_0(Å)	C_{11}	C_{12}	C_{44}	γ_s,110	γ_s,100(J/m^2)	γ_s,123
0.0	2.8668	242.5	145.7	112.4	1.44	1.63	1.65
0.03125	2.8700	235.1	143.3	112.9	1.37	1.53	1.57
0.06250	2.8733	240.1	140.5	111.2	1.34	1.58	1.53
0.09375	2.8767	248.2	139.1	105.6	1.31	1.52	1.50

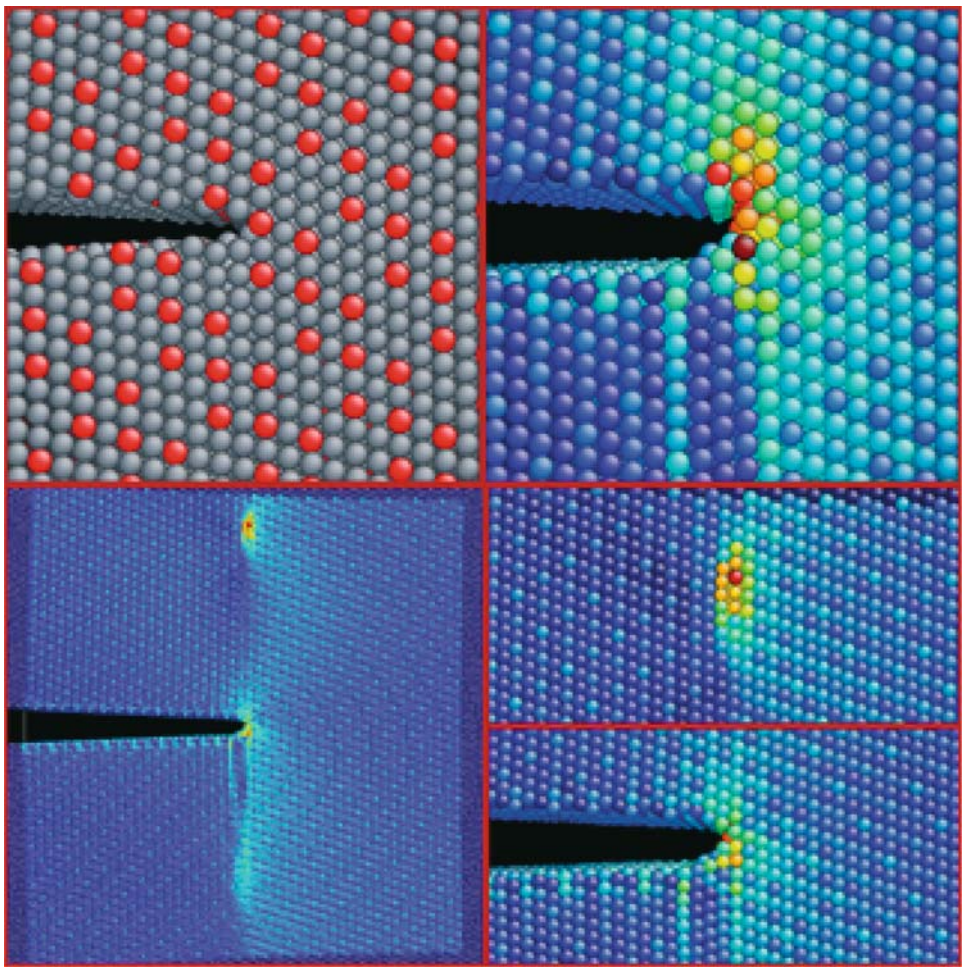

Fig. 6—Configurations of the Fe-9.375 pct Ni system during crack loading in orientation 3. Top left: crack-tip region after initial loading at $K_I = 0.87$ MPa$\sqrt{m}$. The Ni atoms are colored red. Top right: crack-tip region at $K_I = 1.25$ MPa$\sqrt{m}$, just prior to dislocation emission. Atoms colored by Von-Mises stress, ranging from blue (low) to red (high). Bottom left: simulation box at $K_I = 1.27$ MPa$\sqrt{m}$, just after crack tip blunting. Bottom right: closeups of the crack-tip region and {112} edge emitted on a plane 90 deg from the crack plane.

selected configuration during the loading of the Fe-9.375 at. pct Ni system in the same orientation. Here, the mechanical twin grows continuously to a stress intensity nearly 10 pct higher than was found for the pure Fe case (1.25 compared to 1.14 $MPa\sqrt{m}$). The next loading step induces the emission of an edge dislocation along the {112} plane at 90 deg. This evolution—growth of the twin with increasing stress intensity, followed by dislocation emission—was observed for all concentrations considered both for Ni and Cr additions. It does appear, however, that the solute type seems to influence the preferred emission slip system. In the case of Cr, crack blunting by dislocation emission on the {112} plane at $\theta = -19.5$ deg was observed at all solute concentrations. For Ni, similar behavior was seen at 3.125 pct, but at higher concentrations (6.25 and 9.375 at. pct), blunting occurred by emission on the plane at $\theta = 90$ deg.

In orientation 4, the unalloyed Fe system exhibited a ductile response at $K = 1.06\ MPa\sqrt{m}$, simultaneously emitting a pure edge on the {110} plane at 90 deg and a mixed dislocation on the {132} plane at $\theta = -28.1$ deg (*cf.* Figure 4). In this case, addition of Cr caused the crack to cleave on the {132} plane at a stress intensity roughly 10 pct higher (1.14 to 1.15 $MPa\sqrt{m}$). An example of this is depicted for the Fe-3.125 at. pct Cr system in Figure 7. By contrast, Ni additions had almost no effect, giving rise to a nearly identical response to that of the pure Fe system. These trends seem consistent with the observed changes in γ_s on the {123} plane; with Cr addition, the surface energy decreases, which should make cleavage easier, while Ni substitution has almost no effect on γ_s.

In orientation 5, it was found that the addition of Cr and Ni appears to lower the stress intensity for cleavage by about 10 pct. The effect does not appear to be directly related to the bulk concentration of the solute, but rather to the local concentration present in the atomic bonds that break upon crack advance. This is demonstrated in Figure 8; each column depicts the configurations of Fe-Cr systems just prior to and after cleavage. The cleavage stress intensities at 3.125, 6.25, and 9.375 pct are 1.03, 1.12, and 1.07 $\text{MPa}\sqrt{m}$, respectively. In the configurations with 3.125 and 9.375 pct Cr, solute atoms are present in the row of bonds that must break for the crack to advance. These cases both cleave at a lower stress intensity than the solute-free case (*cf.* $K_I = 1.12$ for pure Fe). By contrast, the crack tip in the configuration with 6.25 pct Cr has no Cr in the layer of bonds that have to break, and the stress intensity for crack advance is the same as the pure Fe case. It can be seen from the figure that, upon cleavage, the crack tip

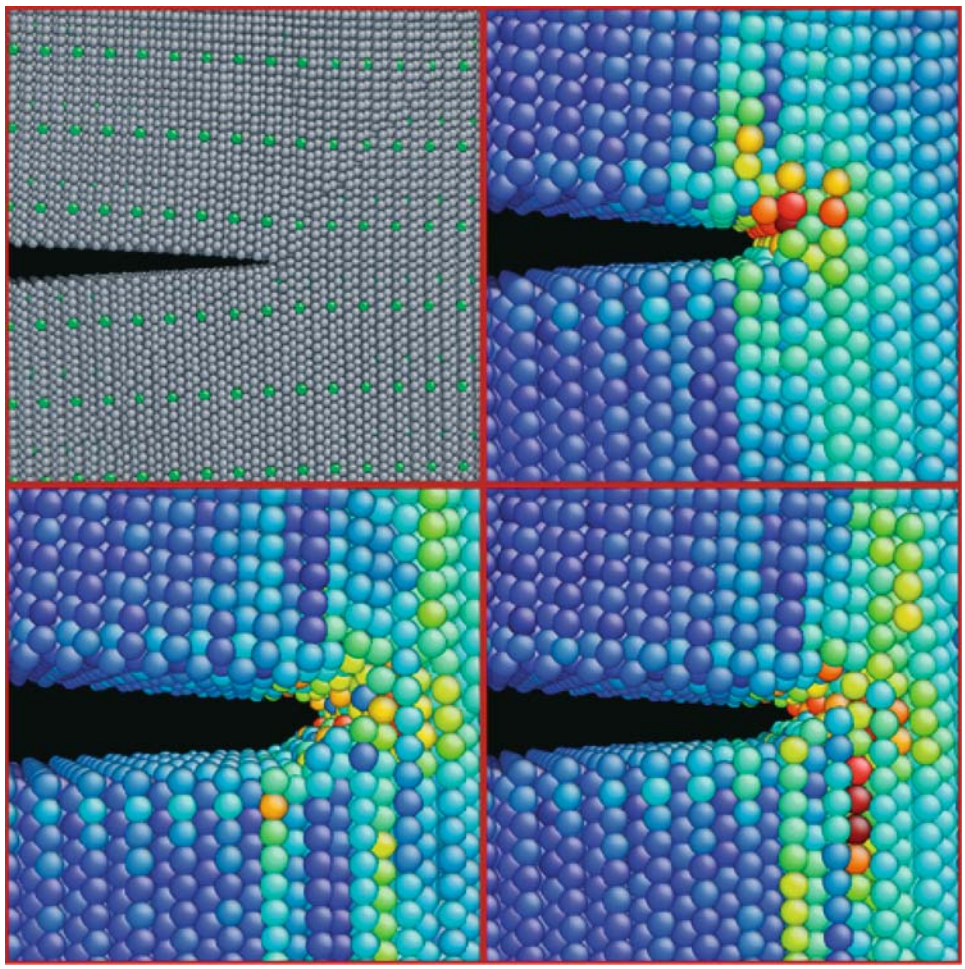

Fig. 7—Configurations of the Fe-3.175 pct Cr system during crack loading in orientation 4. Top left: crack-tip region after initial loading at $K_I = 0.87$ $\text{MPa}\sqrt{m}$. The Cr atoms are colored green. Top right: crack-tip region at $K_I = 1.14$ $\text{MPa}\sqrt{m}$, just prior to cleavage on the (132) plane. Atoms colored as in Fig. 6. Bottom right: crack-tip region at $K_I = 1.15$ $\text{MPa}\sqrt{m}$, just after cleavage. Bottom left: crack-tip region at $K_I = 1.30$ $\text{MPa}\sqrt{m}$.

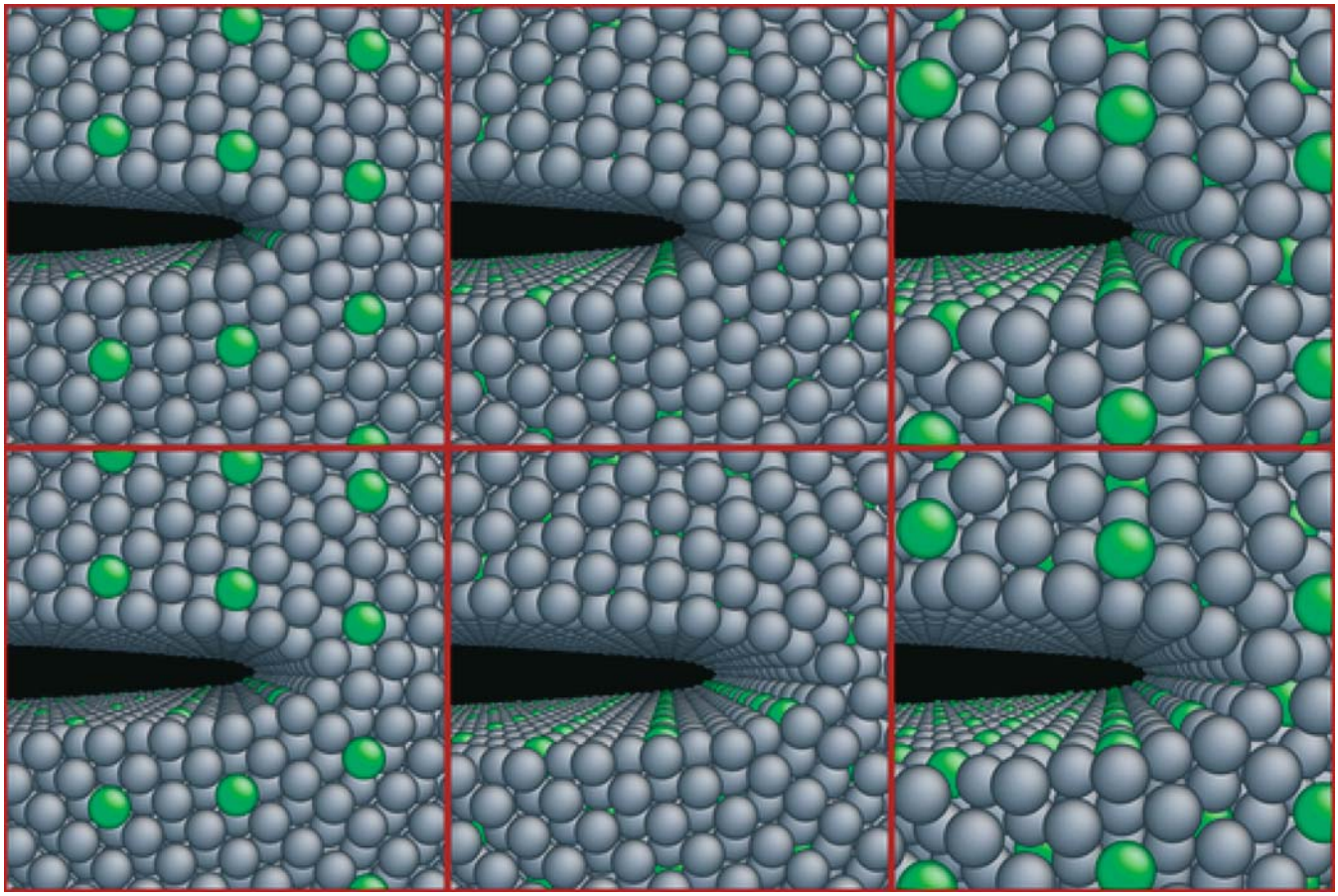

Fig. 8—Configurations of Fe-Cr systems before and after the cleavage event in orientation 5. For each column, the crack-tip configuration just prior to cleavage (top) and just after (bottom) are shown. The Cr atoms are colored green. Left column: 3.125 pct Cr, top: $K_I = 1.01$, and bottom: $K_I = 1.03$. Middle column: 6.25 pct Cr, top: $K_I = 1.11$, and bottom: $K_I = 1.12$. Right column: 9.375 pct Cr, top: $K_I = 1.06$, and bottom: $K_I = 1.07$.

advances several layers forward, whereas in the other cases, exactly one row of bonds breaks. This serves as an argument for the fact that the presence of solutes here modifies the degree of lattice trapping in the system. For both Ni and Cr, the effect appears to be about the same; it is possible that the main effect of the solute in this case is to provide some energetic heterogeneity that eases nucleation of bond breakage, allowing the crack to advance at lower applied stress.

IV. CONCLUSIONS

Molecular statics simulations of mode I loading were conducted on iron single crystals. The failure processes that take place at an atomically sharp crack tip were observed to be a strong function of orientation, exhibiting brittle cleavage, and ductile emission of full dislocations and mechanical twins. Several recently developed interatomic potential models were tested, and overall the crack-tip response was fairly uniform among the different models. Several cases were noted, however, where the crack tip exhibited a qualitatively different response among different EAM models for Fe. This suggests the enormous sensitivity the crack-tip behavior must have to the potential energy surface of the models, particularly at configurations far from the equilibrium configurations for which the models are parameterized.

The Rice criterion for dislocation emission and Griffith criterion for brittle cleavage were applied to the results but were found to be incapable of predicting the failure pathway of the observed crack-tip response. Lattice trapping effects were observed to be present and strongly orientation dependent, obscuring a general correlation of cleavage with surface energy. Based on self-consistently derived unstable stacking fault energies, the Rice theory seems to consistently overestimate the barriers for dislocation emission. The predictions could be improved for both mechanisms. For cleavage, analysis of the activation energy barriers present could be analyzed using techniques such as the nudged elastic band method. Incorporation of surface stress effects or tension-shear coupling could improve the ductile emission prediction.

The effect of Ni and Cr solutes present as ordered substitutional elements was explored and found to qualitatively modify the Fe crack-tip response in several orientations. Although the potentials for the mixed systems must be regarded as very rudimentary, the fact that significant changes can result suggest that more careful attention should be paid to the development of more rigorous mixed system potentials. It is expected that *ab initio* calculations should be of enormous benefit to that end, especially if the effects of other solutes is to be explored.

ACKNOWLEDGMENTS

Special thanks go to Concenzione Halsey, Ruohua Guo, and Youhong Li (ExxonMobil Research & Engineering) for helpful discussions throughout this work.

REFERENCES

1. W. Leslie: *Metall. Trans.*, 1972, vol. 3, pp. 5-25.
2. Y. Chen, D. Atteridge, and W. Gerberich: *Acta Metall.*, 1981, vol. 29, pp. 1171-85.
3. W. Gerberich, Y. Chen, D. Atteridge, and T. Johnson: *Acta Metall.*, 1981, vol. 29, pp. 1187-1201.
4. B. deCelis, A. Argon, and S. Yip: *J. Appl. Phys.*, 1983, vol. 54, pp. 4864-78.
5. K. Cheung and S. Yip: *Modelling Simul. Mater. Sci. Eng.*, 1994, vol. 2, pp. 865-92.
6. V. Shastry and D. Farkas: *Modelling Simul. Mater. Sci. Eng.*, 1996, vol. 4, pp. 1-21.
7. G.J. Ackland, D.J. Bacon, A.F. Calder, and T. Harry: *Phil. Mag. A*, 1997, vol. 75, pp. 713-32.
8. G.J. Ackland, M. Mendelev, D.J. Srolovitz, and A. Barashev: *J. Phys. Condens. Matter*, 2004, vol. 16, pp. S2629-S2642.
9. M.I. Mendelev, S. Han, D.J. Srolovitz, G.J. Ackland, D.Y. Sun, and M. Asta: *Phil. Mag.*, 2003, vol. 83, pp. 3977-94.
10. G. Sih and H. Liebowitz: *Fracture*, Academic Press, New York, NY, 1968, vol. 2, pp. 108-30.
11. R. Hoagland: *Phil. Mag. A*, 1997, vol. 76, pp. 543-63.
12. F. Cleri, S. Yip, D. Wolf, and S.R. Philpot: *Phys. Rev. Lett.*, 1997, vol. 79, pp. 1309-12.
13. G. Simonelli, R. Pasianot, and E. Savino: *Mater. Res. Soc. Symp. Proc.*, 1993, vol. 291, pp. 567-72.
14. A.F. Voter and S. Chen: *Mater. Res. Soc. Symp. Proc.*, 1986, vol. 82, pp. 175-80.
15. D. Farkas, D. Roquueta, A. Vilette, and K. Ternes: *Modelling Simul. Mater. Sci. Eng.*, 1996, vol. 4, pp. 359-69.
16. C. Vailhe and D. Farkas: *Mater. Sci. Eng., A*, 1998, vol. 258, pp. 26-31.
17. J.R. Rice: *J. Mech. Phys. Solids*, 1992, vol. 40, pp. 239-71.
18. D. Farkas, S.J. Zhou, C. Vailhe, B. Mutasa, and J. Panova: *J. Mater. Res.*, 1997, vol. 12, pp. 93-99.
19. J. Li: *Modelling Simul. Mater. Sci. Eng.*, 2003, vol. 11, pp. 173-77.
20. P. Gumbsch and R.M. Cannon: *MRS Bull.*, 2000, vol. 25, pp. 15-20.
21. A. Paskin, D.K. Som, and G.J. Dienes: *J. Phys. C: Solid State Phys.*, 1981, vol. 14, pp. L171-L176.
22. D. Farkas, M. Mehl, and D. Papaconstantolpoulos: *Materials Research Society Symp. Proc.,* 2001, vol. 653, pp. Z6.4.1-Z6.4.6.
23. N. Bernstein and D. Hess: *Phys. Rev. Lett.,* 2003, vol. 91, pp. 022501-1-022501-4.
24. J. Knap and K. Sieradzki: *Phys. Rev. Lett.*, 1999, vol. 82, pp. 1700-03.
25. S. Zhou, A. Carlsson, and R. Thomson: *Phys. Rev. Lett.*, 1994, vol. 72, pp. 852-55.
26. Y. Sun, G.E. Beltz, and J. Rice: *Mater. Sci. Eng., A*, 1993, vol. 170, pp. 67-85.